Astronomy & Astrophysics manuscript no. aanda
November 18, 2025

Infrared Signatures of Dusty Tori Formed by MHD-Driven Outflows

Ruiyu Pan[1] and Arkaprabha Sarangi[2,3]

[1] Niels Bohr Institute, University of Copenhagen, Lyngbyvej 2, 2100 Copenhagen Ø, Denmark
[2] Indian Institute of Astrophysics, 100 Feet Road, Koramangala, Bengaluru, Karnataka 560034, India
[3] DARK, Niels Bohr Institute, University of Copenhagen, Jagtvej 155A, 2200 Copenhagen, Denmark

ABSTRACT

We aim to probe the physical structure and conditions of the central regions of active galactic nuclei (AGN) by interpreting their mid-infrared observational spectra. We constructed a sophisticated three-dimensional radiative transfer model of the AGN source and dusty torus, built upon a physically motivated framework that includes a comprehensive dust grain model. To investigate the properties of the circumnuclear medium, we performed model fitting to a sample of 20 observational spectra from Spitzer Space Telescope's IRS Enhanced Data Products, testing two distinct dust density laws: a steep r^{-2} profile, characteristic of a radiation pressure-driven wind, and a shallower r^{-1} profile, which is a key prediction of magnetohydrodynamic (MHD) models. Our model successfully reproduces fundamental observational phenomena, such as the transition from 9.7 μm silicate emission at low inclinations to deep absorption at high inclinations, with absorption features becoming more pronounced for higher accretion rates, dust-to-gas ratios, and black hole masses. Most importantly, a direct comparison of the fitting results revealed that the r^{-1} density law provided a significantly better fit (χ^2) than the r^{-2} density law for 18 of the 20 observational spectra. These results confirm the physical consistency of our advanced radiative model and provide compelling evidence that an r^{-1} density law is a more accurate representation of the AGN dusty torus.

Key words. galaxies: active – dust, extinction – radiative transfer – MHD – methods: numerical – infrared: galaxies

1. introduction

Interstellar dust plays a crucial role in galaxy evolution by regulating the exchange of energy and matter and reprocessing stellar radiation into the infrared (Draine 2003; Zubko et al. 2004; Hauser & Dwek 2001). Despite its importance, a fundamental tension persists between the observed vast quantities of dust and the limited production capacity of known stellar sources, a mismatch known as the 'dust budget crisis' (Dwek & Cherchneff 2011; Jones & Nuth 2011). This crisis is particularly acute in extreme environments like AGN, where dust not only survives intense radiation and strong outflows but is also central to the AGN unification model. In this framework, an optically thick dusty structure, often called a dusty torus, is responsible for the observational dichotomy between type 1 and type 2 AGNs (Antonucci & Miller 1985; Pier & Krolik 1992).

The classical view of a smooth, monolithic dusty torus in AGNs has been challenged by high-resolution interferometric observations, which instead reveal a clumpy, dynamic, and non-axisymmetric structure (Jaffe et al. 2004; Tristram et al. 2007). The survival and replenishment of these dust clumps in close proximity to the central engine deepen the puzzle of the dust budget. This has motivated sophisticated models that incorporate turbulence, radiation pressure, and magnetic fields to explain the structure and kinematics of the torus (Wada et al. 2009; Elvis et al. 2002). Critically, these findings raise the possibility of in-situ dust formation within the AGN environment itself, moving beyond a sole reliance on stellar ejecta (Chan et al. 2017).

The dust budget crisis is at its most extreme in the early universe. For instance, the quasar SDSS J1148+5251, seen when the universe was very young ($z = 6.4$), contains a staggering dust mass ($M_{\rm dust} \sim 10^8\,M_\odot$), which is about 100 times more than all the stars in that galaxy could possibly have produced (Wang et al. 2023; Valiante et al. 2011). The light from these ancient galaxies shows strong signs of silicate dust, similar to local AGNs, but surprisingly lacks the characteristic spectral features of polycyclic aromatic hydrocarbons (PAHs). (Li et al. 2023). This suggests that most of this early dust was not made in stars at all, but formed rapidly in powerful outflows driven by magnetic fields, an idea that could fundamentally alter our understanding of how the first galaxies grew (Ferrara et al. 2017).

In nearby systems such as NGC 1068, observations provide detailed images of AGN dust structures. Strong 9.7 μm silicate absorption and polarized broad-line emission indicate a geometrically and optically thick dusty torus (Antonucci 1993; Tristram et al. 2007). ALMA observations reveal a ring-shaped magnetic field of ~10 mG driving molecular outflows at velocities up to ~500 km s^{-1}, consistent with magnetocentrifugal wind models (Lopez-Rodriguez et al. 2020; Blandford & Payne 1982a). Similar high-velocity molecular outflows are seen in high-z quasars like Mrk 231, likely driven by both radiation pressure and MHD mechanisms (Aalto et al. 2020; Veilleux et al. 2020; Wada 2012). These outflows are predicted to follow the dust density law $n(r) \propto r^{-1}$ and $v(r) \propto r^{-0.5}$, in agreement with X-ray and IR observational constraints (Fukumura et al. 2018; Behar et al. 2009; Tristram et al. 2007; Sarangi et al. 2019).

Beyond dynamics, AGN dust exhibits distinctive chemical compositions. Crystalline silicates, rare in the general ISM, can reach up to 20% abundance in AGN environments, possibly forming via non-equilibrium condensation in hot outflows (Srinivasan et al. 2017; García-Burillo et al. 2021). Carbonaceous dust is also often enhanced, with elevated C/Si mass ratios and dust-to-gas ratios up to ten times those in the typical ISM (Shi et al. 2006; Gallimore et al. 2016). Recent JWST observations reveal further complexity: 3.3 μm PAH emission is detected in NGC 1068, originating from clumps with $n \sim 10^7$ cm^{-3} and visual extinction $A_V \sim 10$ mag, possibly embedded

in MHD-driven outflows (Donnan et al. 2023; Bogdanović et al. 2021). These findings suggest a multi-component dust structure: silicates dominate mid-IR absorption, carbonaceous grains control UV obscuration, and PAHs contribute to near-IR emission.

The observed infrared emission from a galaxy's circumnuclear region typically has two primary contributors: thermal radiation from AGN-heated dust and light from starburst (SB). Ignoring the contribution from a starburst (SB) can severely bias the interpretation of AGN spectra, as features like PAH emission and the cooler continuum are often misattributed to the central engine. Such contamination distorts key derived properties—including silicate feature strength, viewing angle, and extinction—while also affecting energy budgets and the classification of the system's dominant power source (Genzel et al. 1998; Spoon et al. 2007). Consequently, it has become standard practice to explicitly model the SB component in infrared diagnostics to separate the host and nuclear emission in integrated spectra, thereby reducing systematic errors from component mixing (Laurent et al. 2000; Nardini et al. 2008).

In summary, a comprehensive model of the AGN dusty torus must simultaneously address three key physical components. First, the model must account for the intrinsic dust microphysics, as the grain composition and size distribution directly govern the infrared absorption and emission characteristics (Srinivasan et al. 2017; Shi et al. 2006). Second, it must explicitly disentangle the contribution from circumnuclear star formation to avoid significant biases in derived torus properties such as silicate strength and obscuration (Laurent et al. 2000; Nardini et al. 2008). Finally, the model must incorporate the anisotropic radiation field of the central engine, which is crucial for establishing the dust sublimation boundary and reproducing the polar dust extensions seen in high-resolution observations (Lawrence & Elvis 2010; López-Gonzaga & Jaffe 2016).

The primary contribution of this work is a new suite of 3D radiation-magnetohydrodynamic simulations designed to capture the intrinsic properties of the AGN dusty torus with high fidelity. Our models self-consistently treat the multi-component dust physics and the angle-resolved radiation field from the central engine. To bridge the gap between these theoretical models and observations, we adopt a forward modeling approach. We combine the spectral energy distributions (SEDs) generated by our AGN torus simulations with well-established empirical SB templates. This methodology allows us to robustly decompose the observed infrared emission, separating the intrinsic AGN signal from that of its host galaxy. This, in turn, enables a more accurate determination of the physical properties of the torus, such as its structure, geometry, and composition.

The paper is arranged in the following order. In Section 2 we describe the physical and computational details of our model. In Section 3 we present the results of our simulations, including the application of our models to observational data. Finally, in Section 4, we discuss the implications of our work and present our conclusions.

2. Model description

2.1. AGN

AGNs represent some of the most energetic and luminous phenomena known in the cosmos. Powered by accretion onto supermassive black holes (SMBHs), with masses ranging from 10^6 to 10^{10} $M_\odot$ (Kormendy & Ho 2013), AGNs often outshine their entire host galaxies across all wavelengths (Elvis et al. 1994). Their extreme luminosities, compact sizes—indicated by rapid variability on timescales of hours to days (Rees 1984)—and broad multiwavelength emission make them ideal astrophysical laboratories for probing relativistic physics, accretion dynamics, and galaxy evolution (Netzer 2013).

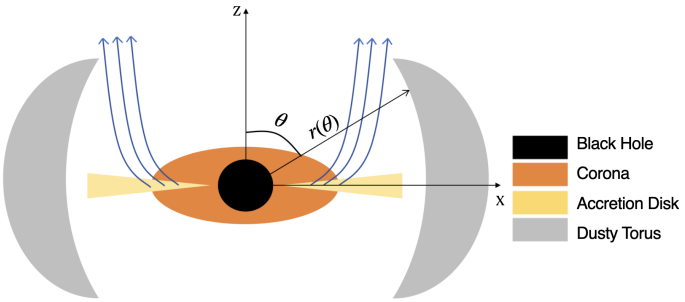

Fig. 1: Simplified 2D schematic of an AGN, illustrating key structural components including the central black hole (black), surrounding hot corona (orange), accretion disk (yellow), and obscuring dusty torus (gray). Blue lines represent the outflowing winds launched from the accretion disk, and $r(\theta)$ is the inner radius of the dusty torus with an inclination angle θ.

Fig. 1 presents a simplified two-dimensional schematic of an AGN. At its core lies an SMBH, whose extreme gravitational potential dominates the dynamics of the surrounding matter. Encircling the SMBH is a geometrically thin, optically thick accretion disk (Shakura & Sunyaev 1973), which extends from the innermost stable circular orbit (ISCO, typically $R_{\rm ISCO} \sim 3R_{\rm sch}$) out to thousands of gravitational radii. This disk efficiently converts gravitational energy into radiation via viscous dissipation. At larger radii, the system transitions into a dusty torus and narrow-line regions, while in the inner disk, magnetic processes may launch powerful relativistic jets (Blandford & Payne 1982b) or winds driven by radiation and MHD forces (Fukumura et al. 2010). The innermost regions, dominated by the SMBH's gravitational potential, are where the majority of the AGN's radiative energy is released.

The intrinsic AGN spectrum is shaped by two primary components: thermal emission from the accretion disk, often referred to as the disk blackbody (dbb), and a non-thermal power-law (pow) from a hot corona, which generates the X-ray continuum via inverse-Compton scattering of disk photons (Shakura & Sunyaev 1973; Haardt & Maraschi 1993). The balance between these two components, often characterized by the optical-to-X-ray spectral index ($\alpha_{\rm OX}$), determines the overall shape of the continuum (Lusso et al. 2016). AGN spectra can also exhibit secondary features, such as a soft X-ray excess and reflection components from the inner disk (Done et al. 2012; Reynolds 2013).

The AGN emission is intrinsically anisotropic due to the combined influence of the geometrical configuration of the accretion disk and the optical depth distribution of the surrounding material. Radiation is preferentially emitted along the polar axis, while emission toward equatorial viewing angles is either significantly attenuated or entirely obscured by optically thick structures. This angular dependence can be parameterized by the following expression for the emergent luminosity,

$$L(\theta) = \eta \dot{m} L_{\rm Edd}(M_8) f(\theta), \quad (1)$$

where η denotes the radiative efficiency (typically ranging from 0.1 to 1), and $\dot{m} = \dot{M}/\dot{M}_{\rm Edd}$ is the normalized accretion rate. The Eddington accretion rate is defined as $\dot{M}_{\rm Edd} = L_{\rm Edd}/c^2$, with

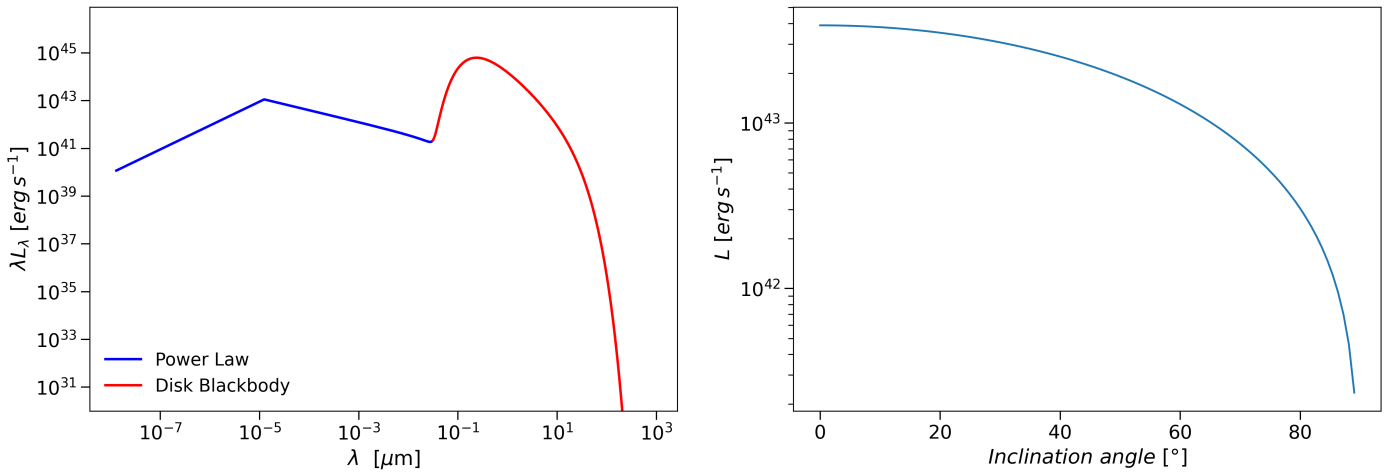

Fig. 2: Left panel: spectral energy distribution of the central AGN source at an inclination angle of $\theta = 75°$. The spectral shape, characterized by $\alpha_{ox} = -1.5$, remains consistent across all viewing angles (Sarangi et al. 2019). The surrounding material is entirely heated by the central AGN radiation. right panel: angle-dependent luminosity function, following the luminosity profile defined in Eq. (2), showing how the observed emission varies with inclination angle due to anisotropic radiation effects.

$L_{\rm Edd}$ representing the Eddington luminosity, which scales linearly with the black hole mass $M_{\rm BH}$. For convenience, the black hole mass is expressed in units of $M_8 = M_{\rm BH}/10^8 M_\odot$ (Sarangi et al. 2019). The angular modulation is described by (Netzer 1987; Stalevski et al. 2012)

$$f(\theta) = \frac{1}{3}\cos\theta\,(1 + 2\cos\theta)\,, \tag{2}$$

which reflects the anisotropic radiation pattern resulting from both disk geometry and radiative transfer effects. The function peaks along the polar direction ($\theta = 0$) and decreases toward the equatorial plane ($\theta = \pi/2$), leading to a substantial inclination dependence of the observed luminosity. While the SED remains approximately invariant in shape across different lines of sight, the bolometric output exhibits significant angular modulation governed by $f(\theta)$ (see Fig. 2).

Our model explores a grid of physical parameters to cover a representative range of AGN properties, as summarized in Table 2. The central supermassive black hole mass spans from 10^6 to 5×10^8 $M_\odot$, with a normalized accretion rate ($\dot{m}$) ranging from 0.1 to 1. We adopt a constant radiative efficiency of $\eta \sim 0.3$. For reference, the Eddington luminosity for a typical black hole mass of 10^7 $M_\odot$ is $L_{\rm Edd} \sim 1.3 \times 10^{45}$ erg s^{-1}.

The AGN spectrum (Fig. 2) is normalized for a viewing angle of 75°, with $\alpha_{\rm OX} = -1.5$. While the spectral shape remains invariant with inclination, the total luminosity scales with $L(\theta)$ (Eqs. (1) and (2)).

2.2. Dust in the dusty torus

The dusty torus in AGN is located close to the central engine and is subject to intense radiation fields. With a typical spatial extent of only a few tens of parsecs, direct observational constraints on the dust composition, size distribution, and spatial structure remain limited due to current resolution capabilities. Although recent advances in infrared interferometry and high-resolution imaging have improved our understanding of the torus morphology, detailed information about the physical nature of the dust grains remains elusive.

Given these observational limitations, many theoretical models have historically relied on simplified dust properties analogous to those of the diffuse ISM. These typically consist of a mixture of silicate and amorphous carbon grains, following the standard Mathis, Rumpl, and Nordsieck (MRN) power-law size distribution ($n \propto a^{-3.5}$) (Mathis et al. 1977). While these simplified, ISM-like dust models do not capture the full complexity of AGN environments, they provide a robust baseline for isolating the effects of other key parameters. By establishing a physically motivated foundation that can reproduce the average AGN SED, such models are ideal for exploring the impact of torus geometry and the radiation field. Therefore, in this study, we adopt a standard ISM-based dust model to specifically investigate how changes in the torus structure and its irradiation shape the emergent infrared emission.

2.2.1. Dust properties

We adopt the dust composition model proposed by Hensley & Draine (2023), originally developed for the diffuse ISM. Despite the different physical conditions in AGN environments, ISM-based dust models remain widely used in torus modeling due to their well-characterized optical properties and ability to reproduce key infrared features (e.g., Fritz et al. 2006; Draine & Li 2007; Nenkova et al. 2008).

In this model, dust grains consist of two main components: Astrodust and PAHs. Astrodust, as described by Draine & Hensley (2021) and summarized in their Table 2, accounts for the bulk of the grain mass and includes amorphous silicates, metallic iron and iron sulfide, carbon, and PAHs. The adopted material densities are $\rho_{\rm Ad} = 2.74$ g cm^{-3} for Astrodust and $\rho_{\rm PAH} = 2$ g cm^{-3} for PAHs. The mass fraction of PAHs is $X_{\rm PAH} = 9.3\%$, with a number fraction of $f_{\rm PAH} = 12.8\%$.

PAHs exist in both neutral and ionized forms, with their charge state depending on grain size. Following Hensley & Draine (2023), the number fraction of ionized PAHs as a function of grain radius a (in angstroms) is given by

$$f_{\rm ion}(a) = 1 - \frac{1}{1 + a/10\ \text{Å}}, \tag{3}$$

indicating that smaller PAHs are more likely to be neutral, while larger ones are predominantly ionized.

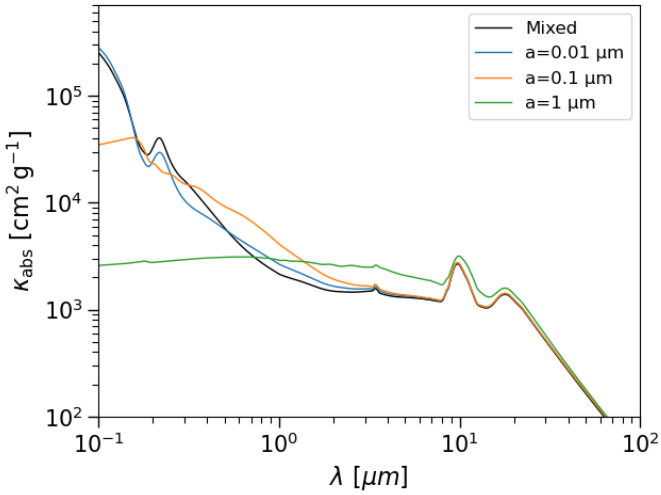

Fig. 3: Mass absorption coefficient κ_{abs} as a function of wavelength for different grain sizes, 0.01μm (blue), 0.1μm (yellow), 1μm (green) and a mixed population (black), including contributions from Astrodust and PAH components (Hensley & Draine 2023).

Table 1: Feature peaks and absorption coefficients of the PAHs+Astrodust model.

Wavelength (μm)	Component	κ_{abs} (cm^2 g^{-1})
0.22	Graphite	40377
3.39	PAH	1577
6.87	PAH	1248
9.78	Silicate	2678
17.92	Silicate	1387

For our radiative transfer calculations, we describe the properties of the dust using the mass-weighted absorption coefficient, which is given by:

$$\kappa_{\rm abs}(\lambda) = \sum_j \sum_i w_{ij}^m \kappa_{\rm abs}^{(j)}(a_i, \lambda), \tag{4}$$

where the sum is performed over all dust components (j) and grain sizes (i), and w_{ij}^m is the mass-weighted number fraction given by

$$w_{ij}^m = \frac{X_j \cdot m_j(a_i) \cdot n(a_i)}{\sum_j \sum_i X_j \cdot m_j(a_i) \cdot n(a_i)}, \tag{5}$$

with X_j being the mass fraction of component j, $m_j(a_i)$ the mass of a grain of size a_i.

Fig. 3 presents the absorption coefficient $\kappa_{\rm abs}$ for various grain sizes as well as for the full grain population following the adopted size distribution. The results show that small grains dominate the extinction at short wavelengths due to their high surface-to-mass ratio, whereas larger grains contribute more significantly at longer wavelengths, especially in the infrared.

Table 1 lists the peak positions and mass absorption coefficients of the key spectral features in the Astrodust+PAHs model. These features, including prominent PAH and broad silicate bands, are essential for interpreting infrared observations and for modeling dust radiative transfer in AGN environments.

2.2.2. Dusty torus geometry

The geometry of the dusty torus is primarily governed by the physical conditions required for dust survival and by dynamical constraints imposed by the environment. The innermost boundary of the dusty structure is set by the dust sublimation radius, which corresponds to the location where the heating and cooling of dust grains are in radiative equilibrium. Dust grains can survive at this radius provided their temperature does not exceed the sublimation threshold (Dwek 1987).

The radiative heating rate of dust grains at a distance D from the central source and at an inclination angle θ is given by

$$H_d(\theta, D) = \int \bar{m}\kappa_{\rm abs}(\lambda)\frac{L_\lambda^s(\lambda,\theta)}{4\pi D^2}d\lambda, \tag{6}$$

where $\bar{m}$ is the average mass and $L_\lambda^s(\lambda,\theta)$ is the monochromatic luminosity of the central source as seen from angle θ. The corresponding cooling rate due to thermal re-emission is

$$L_d(T_d) = \int 4\pi\bar{m}\kappa_{\rm abs}(\lambda)B_\lambda(\lambda, T_d)d\lambda, \tag{7}$$

where $B_\lambda(\lambda, T_d)$ is the Planck function at the dust temperature T_d. By equating the heating and cooling terms, the dust sublimation radius for a temperature of T_d = 1500K can be expressed as

$$R_{1500K}(\theta) = \sqrt{\frac{\int \bar{m}\kappa_{\rm abs}(\lambda)L_\lambda^s(\lambda,\theta)d\lambda}{4\pi L_d(1500{\rm K})}}. \tag{8}$$

This defines the minimum radius at which dust grains can remain thermally stable without sublimating under the incident radiation field. A sublimation temperature $T_{\rm sub}$ = 1500 K is adopted throughout. The sublimation zone, defined by $T_{\rm dust} \geq$ 1500 K, is clearly separated from the condensation zone ($T_{\rm dust} <$ 1500 K) by a distinct boundary. Dust formation and survival are only permitted in the condensation zone, where thermal conditions allow for stable grain existence.

The outer radius of the torus is constrained by the inflow-outflow equilibrium condition and is estimated as

$$R_{\rm inf} \sim R_{\rm Sch}\left(\frac{c}{\sigma}\right)^2, \tag{9}$$

where $R_{\rm Sch}$ is the Schwarzschild radius of the central SMBH, c is the speed of light, and σ is the stellar velocity dispersion. For this work, we adopt σ = 200 km s^{-1}, following Forbes & Ponman (1999). The torus is assumed to be axisymmetric, defining a half-opening angle θ_{open} = 20°. The polar regions ($\theta <$ 20°) are therefore considered dust-free, as this zone is dominated by powerful magnetically driven winds that have passed the Alfvén surface and would expel or destroy any grains, in agreement with MHD wind models (Fukumura et al. 2010).

2.2.3. Dust spatial distribution

The spatial distribution of dust in the torus is a key factor in determining both its geometry and radiative properties. However, the dust does not exist in isolation—it is embedded within gas that controls the dynamical and density structure of the torus. In particular, in wind-driven torus models, the dust is assumed to be well-mixed with gas and dynamically coupled to it via radiation pressure and magnetic forces. Therefore, to model the dust distribution in a physically consistent way, we begin by specifying

the gas density structure, and then infer the corresponding dust density through a fixed dust-to-gas mass ratio (DGR).

To describe the gas distribution, we adopt a prescription based on the MHD wind solution presented by Fukumura et al. (2010), which has been shown to reproduce X-ray absorber column densities (e.g. Holczer et al. (2007)). In this model, the gas is launched from the accretion disk in a self-similar outflow, with a density law that follows a power-law $n(r) \propto r^{-1}$, and an angular dependence derived from the wind streamlines.

We define the dimensionless radius as $X = r/R_{\rm sch}$, where the Schwarzschild radius is given by

$$R_{\rm sch} = 3 \cdot 10^{13}\ M_8\ {\rm cm}, \tag{10}$$

with M_8 being the black hole mass in units of $10^8\ M_\odot$. The gas number density is then expressed as

$$n(r,\theta) = n_0 \frac{\dot{m}}{M_8} X^{-1} \exp\left[\frac{5}{2}\left(\theta - \frac{\pi}{2}\right)\right], \tag{11}$$

where $n_0 = 5 \times 10^{10}\ {\rm cm}^{-3}$ is a normalization constant, and θ is the polar angle (Sarangi et al. 2019). This form ensures that the radial Thomson optical depth scales with $\dot{m}$, and that the density peaks near the equatorial plane ($\theta = \pi/2$), decreasing toward the poles.

Observational and theoretical studies indicate that in dusty, shielded regions ($A_V \gtrsim 1$, $T \lesssim 10^3$ K) hydrogen contains nearly all of the gas mass and is predominantly neutral, with typical ionization fractions $x_e \equiv n_e/n_{\rm H} \sim 10^{-4}$–$10^{-6}$ (Tielens 2005; Draine 2011; Osterbrock & Ferland 2006; Netzer 2013). Motivated by this, we identify the modeled gas number density with the hydrogen nuclei number density, $n(r,\theta) \equiv n_{\rm H}(r,\theta)$. The local dust mass density can be written as

$$\rho_{\rm dust}(r,\theta) = \mathcal{D} \cdot m_{\rm H} \cdot n(r,\theta), \tag{12}$$

where $\mathcal{D}$ is the DGR, which we vary from a typical value of 10^{-2} to 10^{-4} to cover a wide range of astrophysical conditions, from solar-metallicity environments (Draine & Li 2007) to those found in low-metallicity galaxies and the early universe (Rémy-Ruyer et al. 2014; Valiante et al. 2011). This expression provides a spatially varying dust density distribution consistent with the underlying gas dynamics, which serves as the foundation for the radiative transfer modeling in the following sections. The complete grid of physical parameters used to construct our models is summarized in Table 2.

Table 2: Model Parameters

Parameter	Adopted values
$M_{\rm BH}$	10^6, 5×10^6, 10^7, 5×10^7, 10^8, $5\times10^8 M_\odot$
$\dot{m}$	0.1, 0.3, 0.5, 0.8, 1.0
$log\mathcal{D}$	-2.0, -2.2, -2.4, -2.6, -2.8, -3.0, -3.2, -3.4, -3.6, -3.8, -4.0
η	0.3
$\alpha_{\rm OX}$	-1.5
θ_{open}	20°
θ_{view}	20°, 40°,60°, 80°
R_{in}	R_{1500K}
R_{out}	R_{inf}
σ	200 $km\ s^{-1}$

2.2.4. Dust extinction and emission

Dust plays a central role in shaping the radiative output of AGNs through its interaction with the central source's emission, both by attenuating incoming radiation via extinction and by re-emitting absorbed energy in the infrared. In this work, we adopt a unified dust model including Astrodust+PAHs, with size distributions and optical constants described before, allowing for calculations of both extinction and emission. Dust extinction arises from absorption and scattering processes, with the wavelength dependence primarily determined by grain size. Small grains, such as PAHs, dominate the ultraviolet regime and are responsible for features like the 2175 Å bump, while larger grains contribute more significantly in the optical and near-infrared.

Dust extinction, which comprises both absorption and scattering, attenuates the radiation from the central source. The total effect is quantified by the mass-weighted extinction coefficient, $\kappa_{ext}(\lambda)$. This coefficient is calculated in the same way as the absorption coefficient (Eq. (4)), simply by using the extinction coefficient in the mass-weighted sum. The optical depth, τ_λ , for a given dust mass column density, Σ_d , is then given by:

$$\tau_\lambda = \kappa_{\rm ext}(\lambda) \cdot \Sigma_d, \tag{13}$$

where Σ_d is the dust mass column density along the line-of-sight. This extinction curve reproduces the key spectral features observed in AGNs, including the prominent silicate absorption bands at 9.7 and 17.9 μm, and serves as a critical input for radiative transfer modeling.

When dust grains absorb incident radiation, they heat up and re-emit the energy thermally in the infrared, reaching a state of radiative equilibrium. The resulting emission spectrum is primarily determined by the dust temperature, T_d, which in turn depends on the dust size and composition, as well as the intensity and angle of the local radiation field. The total thermal emission from the dust population is not a perfect blackbody. We therefore model its radiative luminosity, $L_\lambda^{\rm dust}(\lambda)$, using a modified blackbody formalism:

$$L_\lambda^{\rm dust}(\lambda) \propto \kappa_{\rm abs}(\lambda) B_\lambda(\lambda, T_d), \tag{14}$$

where $B_\lambda(\lambda, T_d)$ is the Planck function and the wavelength-dependent absorption coefficient. Here, the absorption coefficient $\kappa_{\rm abs}$ acts as a wavelength-dependent emissivity, which modifies the Planck function, generally being less efficient at longer wavelengths.

The spatial distribution of dust temperature is determined by the anisotropic radiation field of the AGN and the geometric structure of the torus. As shown in Fig. 6, the dust sublimation boundary is defined by regions where $T_{\rm dust} \geq 1500$ K, beyond which grains cannot survive. Only in the outer condensation zone, where temperatures fall below this threshold, are dust grains thermally stable. By integrating the emission over the full grain population and spatial extent of the torus, we obtain the emergent infrared SED, which reflects both the radial temperature gradient and angle-dependent heating by the central engine. While the current model omits effects such as stochastic heating, grain growth, or destruction mechanisms, it provides a physically motivated and self-consistent framework for interpreting the infrared emission from AGN dusty tori. The limitations and possible extensions of this approach are discussed further in Section 4.

2.2.5. The comparative r^{-2} model

The radial density law, $n(r) \propto r^{-\alpha}$, is a key diagnostic of the gas dynamics within the AGN torus, and it also influences the distribution of dust. In this study, we contrast two physically motivated scenarios: (i) our fiducial model with a shallower gradient ($\alpha = 1$), consistent with accelerating wind simulations (see Sect. 2.2.3; Fukumura et al. 2010; Behar et al. 2009), and (ii) a comparative model with a steeper gradient ($\alpha = 2$), motivated by models of a radiation pressure-driven wind that has reached a constant-velocity outflow (Elvis 2000). This comparison allows us to quantify how key observational signatures are affected by the assumed wind properties.

To ensure a fair comparison, all other physical and geometric parameters of the model (e.g., black hole mass, accretion rate) are held identical to those in our fiducial r^{-1} model. Instead, we derive the r^{-2} profile by requiring that the radial column density, $N_{\rm gas}(\theta) = \int_{R_{1500\rm K}(\theta)}^{R_{\rm inf}} n(r,\theta)\, dr$, is conserved at each polar angle θ between the two models. This constraint ensures that an observer's line-of-sight at any given inclination intercepts the same total amount of gas integrated along the radial path. By equating the column densities, we can express the number density for the r^{-2} model directly in terms of the parameters from our fiducial model:

$$n(r,\theta) = \mathcal{N}(\theta)\, n_0\, \frac{\dot{m}}{M_8} X^{-2} \exp\left[\frac{5}{2}\left(\theta - \frac{\pi}{2}\right)\right], \tag{15}$$

where the normalization factor $\mathcal{N}(\theta)$, which ensures column density conservation, is given by

$$\mathcal{N}(\theta) = \frac{R_{\rm inf} R_{1500\rm K}(\theta) \ln(R_{\rm inf}/R_{1500\rm K}(\theta))}{R_{\rm inf} - R_{1500\rm K}(\theta)}. \tag{16}$$

All parameters in Eq. (15)(e.g., n_0, $\dot{m}$, M_8) are identical to those in Eq. 11. The new normalization factor $\mathcal{N}(\theta)$, defined in Eq. (16), ensures that the column density is conserved between the two models. This approach avoids introducing new fundamental constants and provides a self-consistent framework for comparing the impact of the density gradient. In Sect. 3.2, we will compare the results from this r^{-2} model with our fiducial (r^{-1}) model to determine how the radial density gradient affects key observational signatures.

2.3. Starburst

Table 3 lists the J2000 coordinates and systemic redshifts (z) of the galaxies used as SB templates in this work. With the exception of Arp 220, M 82, and NGC 253, all objects are selected from the Spitzer/IRS starburst sample of Brandl et al. (2006) and are classified there as starburst-dominated systems. In our analysis, these templates provide only the SED shapes; the absolute normalization is determined during the fit to each target.

In addition, we include three well-studied systems—Arp 220, M 82, and NGC 253—as representative SB templates. Arp 220 is an ultraluminous infrared galaxy (ULIRG), $L_{\rm IR} \gtrsim 10^{12}\, L_\odot$, from a late-stage merger with extreme dust obscuration and a very compact nuclear starburst; its mid-IR shows deep 9.7 μm silicate absorption and weak apparent PAH features, and its SED peaks sharply in the far-IR (Sanders & Mirabel 1996; Downes & Solomon 1998; Polletta et al. 2007). M 82 is the nearby prototypical starburst, with strong PAH emission, prominent mid-IR fine-structure lines, moderate silicate absorption, and a relatively warm far-IR color; we follow common empirical representations (Silva et al. 1998; Förster Schreiber et al. 2003; Polletta et al. 2007). NGC 253 is a nearby dusty nuclear starburst with strong PAH features and bright far-IR/submillimeter emission; its Spitzer/IRS spectrum places it firmly among starburst-dominated systems (Brandl et al. 2006; Radovich et al. 2001; Dale et al. 2012). Together these three templates span a useful range of obscuration, PAH strength, and dust temperature, and thus provide complementary SED shapes for our fits.

Fig. 4 compares these three representative SB templates—Arp 220, M 82, and NGC 253—after uniform preprocessing and normalization. All spectra have been shifted to the rest frame and resampled onto our fitting wavelength grid. For visualization, each template is normalized by its rest-frame flux density at 25 μm, $F_{\rm norm}(\lambda) = F_\lambda(\lambda)/F_\lambda(25\,\mu{\rm m})$, so that the

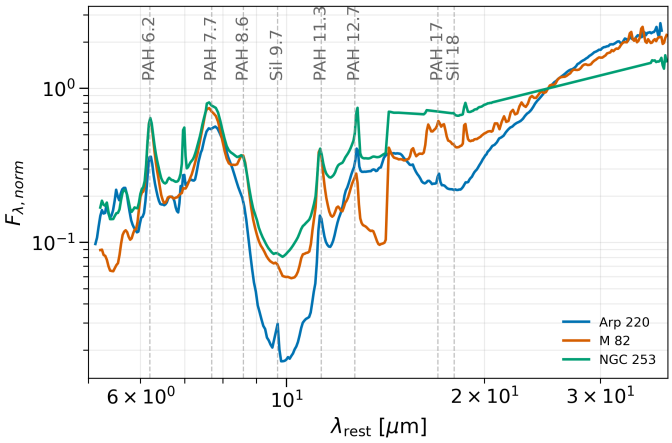

Fig. 4: Rest-frame mid-infrared starburst templates used in this work. Normalized F_λ spectra of Arp 220 (blue), M 82 (orange), and NGC 253 (green) are shown as a function of $\lambda_{\rm rest}$. Prominent PAH complexes at 6.2, 7.7, 8.6, 11.3, 12.7, and 17μm and the silicate absorption features at 9.7 and 18 μm are indicated by vertical dashed lines.

Table 3: SB reference objects

Object	RA (J2000)	Dec (J2000)	z
Arp 220	15:34:57.2	+23:30:11	0.0181
IC 342	03:46:48.5	+68:05:46	0.0001
M 82	09:55:52.7	+69:40:46	0.0007
Mrk 52	12:25:42.7	+00:34:20	0.0079
NGC 253	00:47:33.1	−25:17:18	0.0008
NGC 520	01:24:35.1	+03:47:33	0.0076
NGC 1222	03:08:56.7	−02:57:18	0.0081
NGC 1614	04:33:59.8	−08:34:44	0.0159
NGC 2146	06:18:37.7	+78:21:25	0.0030
NGC 2623	08:38:24.1	+25:45:17	0.0185
NGC 3256	10:27:51.3	−43:54:13	0.0094
NGC 3310	10:38:45.9	+53:30:12	0.0033
NGC 3556	11:11:31.0	+55:40:27	0.0023
NGC 4088	12:05:34.2	+50:32:21	0.0025
NGC 4194	12:14:09.6	+54:31:35	0.0083
NGC 4676	12:46:10.1	+30:43:56	0.0220
NGC 4818	12:56:48.9	−08:31:31	0.0025
NGC 7252	22:20:44.8	−24:40:42	0.0159
NGC 7714	23:36:14.1	+02:09:19	0.0093

Notes. Values compiled from commonly used NED/SIMBAD entries and rounded.

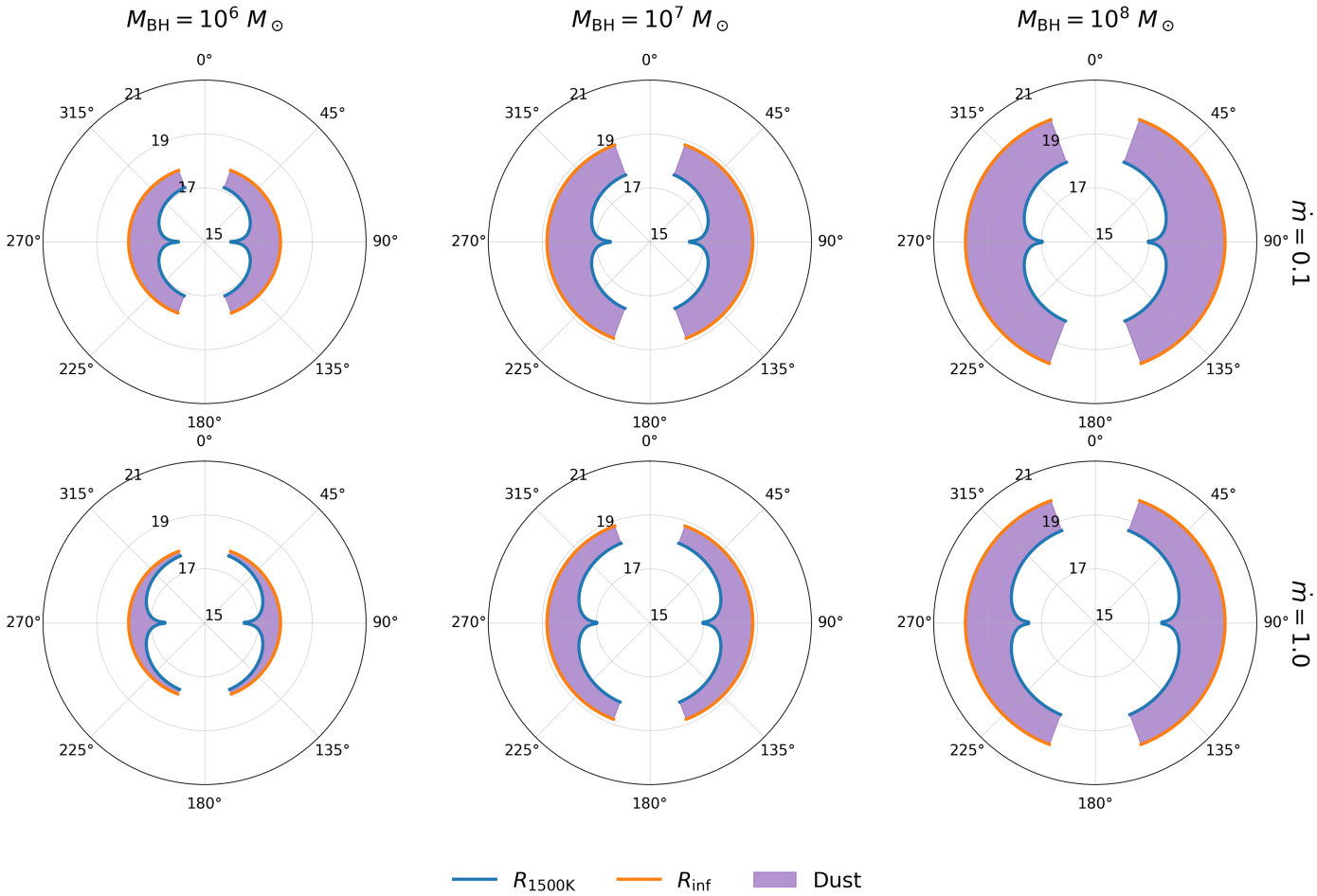

Fig. 5: Polar diagrams illustrating the spatial distribution of AGN dusty torus under varying black hole masses and accretion rates. The panels in the first row correspond to an accretion rate of $\dot{m} = 0.1$, while those in the second row correspond to $\dot{m} = 1$. From left to right, the black hole mass increases from $10^6 M_\odot$ to $10^8 M_\odot$. The radial extent and angular coverage of the dust (purple shading) are shown, overlaid with the sublimation radius at 1500 K (R_{1500K}, blue line) and the outer boundary of the torus (R_{inf}, orange line).

curves intersect at unity at 25 μm; the absolute scaling is free in the fits. Vertical dashed lines mark the principal PAH and silicate features.

In practice, Arp 220 anchors the heavily obscured end (deep 9.7 μm silicate, weak apparent PAHs), M 82 anchors the PAH-strong, warmer continuum end, and NGC 253 lies in between with a flatter 15–30 μm continuum. Minor discontinuities near 14 μm reflect the IRS SL/LL stitch and are absorbed by the covariance in our fits. This compact SB basis improves robustness in separating starburst and AGN components.

3. Results

3.1. Spatial and temperature distribution

This section presents the spatial and thermal distribution of the dusty torus under varying black hole masses and accretion rates. We employed a two-dimensional radiation-MHD model incorporating multi-component dust composition and anisotropic radiation fields to simulate the morphology and temperature distribution of AGN circumnuclear dust. Figs. 5 and 6 display the resulting dust spatial and temperature distributions, respectively.

Fig. 5 shows the polar distribution of dust for black hole masses $M_{BH} = 10^6$, 10^7 and 10^8 $M_\odot$ at accretion rates $\dot{m} = 0.1$ and 1.0. The purple regions represent the dusty zone. The solid blue curve marks the dust sublimation front at $T_{dust} = 1500$ K (R_{1500K}), and the orange curve indicates the outer dynamical boundary R_{inf}, which is determined from the stellar velocity dispersion and represents the black hole's sphere of influence (as defined in Section 2.2.2).

The model reveals that, at a fixed accretion rate, increasing M_{BH} expands both the sublimation radius and the outer boundary, indicating that stronger gravitational potential leads to an overall enlargement of the dusty structure. At fixed M_{BH}, higher accretion rates significantly alter the angular distribution of dust. In the high accretion case ($\dot{m} = 1$), the polar regions are strongly evacuated, and the outer dust zone exhibits a pronounced funnel-like geometry. This polar evacuation is consistent with enhanced MHD-driven winds at high $\dot{m}$, suggesting that the combined effects of radiation and magnetic fields are critical in shaping the torus under such conditions.

Fig. 6 further illustrates the dust temperature distribution for the same set of models. The thermal maps reveal a strong anisotropy in radiative heating: dust temperatures near the polar axis are significantly higher than those in equatorial regions. As a result, the sublimation front is located at a larger radius along the polar axis compared to the equatorial plane, creating a distinctly concave, bowl-like geometry. This anisotropic temperature structure arises directly from the angular dependence of

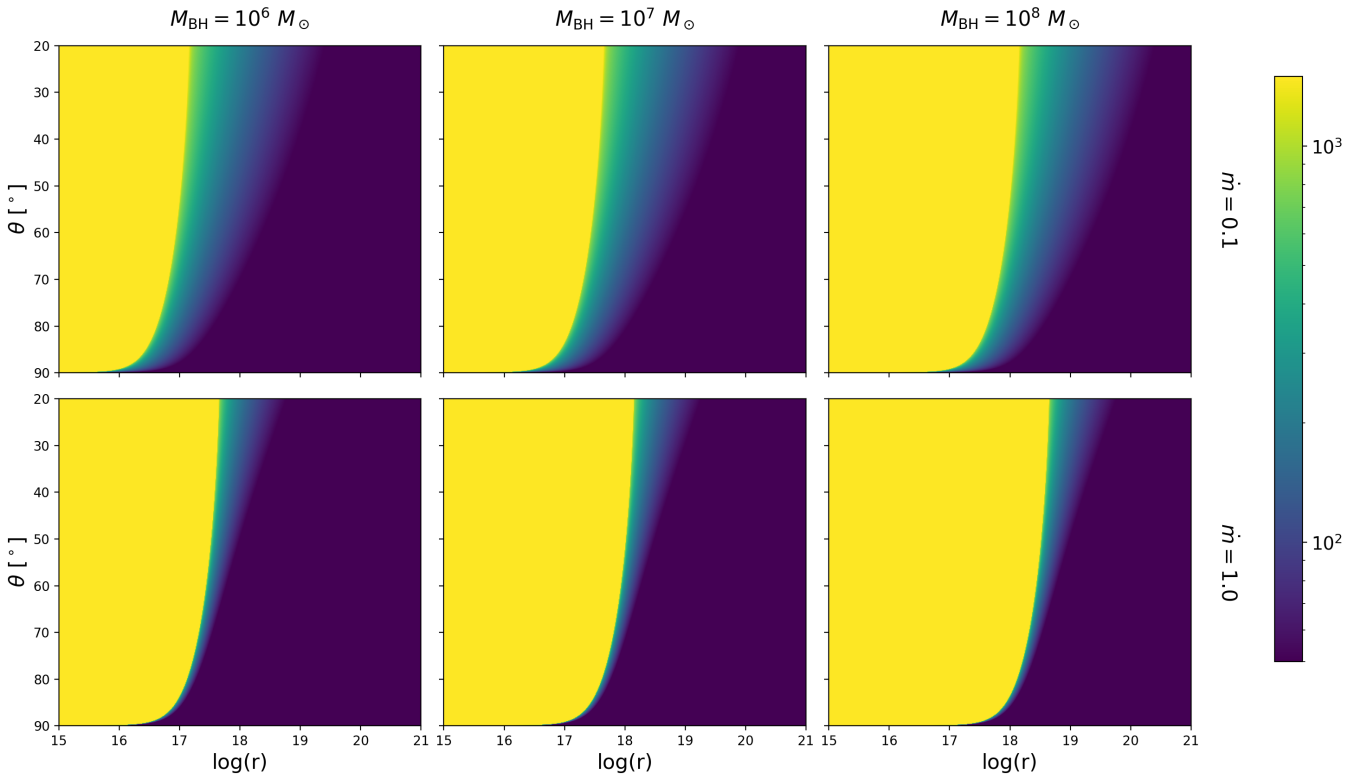

Fig. 6: Two-dimensional temperature maps of radial distance (from $10^{15} cm$ to $10^{21} cm$) and inclination angle (20° to 90°). The top row corresponds to an accretion rate $\dot{m}$ = 0.1, while the bottom row represents an accretion rate $\dot{m}$ = 1. From left to right, the columns show black hole masses of 10^6, 10^7 and $10^8 M_\odot$ respectively. Yellow regions represent temperatures above 1500 K (the dust sublimation threshold), while darker colors (e.g., deep blue) correspond to progressively lower temperatures, down to 0 K.

the central engine's radiation flux (see Eq. (2)), indicating that dust heating is inherently directional.

Taken together, Figs. 5 and 6 demonstrate that the three-dimensional anisotropic radiation field, in concert with wind-driving mechanisms, governs both the geometry and thermal structure of the dusty torus. The sublimation front exhibits marked non-spherical asymmetry, which is crucial for interpreting the infrared SEDs and the polar-extended dust components observed in mid-IR interferometry.

3.2. Model SED library

The core of this research lies in the application of a meticulously constructed, physically motivated library of AGN torus models to interpret observational data. This library covers an extensive parameter space, with six M_{BH} from 1×10^6 to $5 \times 10^8 M_\odot$, and with the normalized accretion rate ($\dot{m}$), dust-to-gas ratio (DGR), and viewing angle (θ_{view}) varied across astrophysically realistic ranges. This model library is not merely a fitting tool; it is our primary probe into the physical conditions of the central regions of AGN.

Fig. 7 presents some infrared SED instances from our AGN torus models, highlighting how viewing angles and dust jointly shape the spectrum. For a fixed black hole mass, accretion rate, and varying dust-to-gas ratio, the near face-on spectra (solid lines) are bright and relatively flat across the mid-IR, while the edge-on spectra (dashed lines) are fainter and develop pronounced silicate absorption around 9.7 μm due to increased obscuration along the line-of-sight. At higher DGR (log $\mathcal{D}$ = -2.0, red), the contrast between face-on and edge-on views is strong, producing deeper absorption and larger overall anisotropy, whereas at lower DGR (log $\mathcal{D}$ = -3.6, blue) the spectra from different viewing angles converge, indicating a more optically thin torus.

As it is impractical to display the full multi-dimensional parameter space, we choose to present and analyze in depth a single, highly representative model grid, shown in Fig. 8. This grid is calculated for a fixed black hole mass of $M_{BH} = 10^8 M_\odot$, a common mass scale for AGN capable of powerful feedback and activity. By analyzing this grid, we can not only understand the fundamental behavior of our model but also reveal the profound diagnostic power of the infrared spectrum, which directly reflects the core physical processes described in the AGN Unified Model. Fig. 8 systematically illustrates how three key physical parameters shape the resulting spectral features.

1. Viewing Angle and the AGN Unification Model: The viewing angle serves as the bridge between different classes of AGN, an effect strikingly illustrated in our model grid. For near face-on views (θ_{view} = 20° – 40°), our line-of-sight probes the hot, inner regions of the torus, resulting in a bright, emission-dominated infrared continuum characteristic of Type 1 AGN. As the viewing angle increases, our line-of-sight is progressively intercepted by the cooler, denser dust. At intermediate angles ($\theta_{view} \approx 60°$), we can see the 9.7 μm silicate feature transitioning from weak emission to flat or even shallow absorption. Finally, for near edge-on

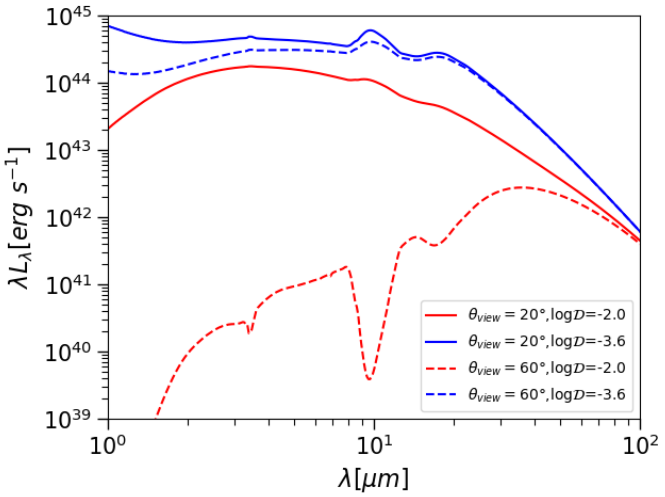

Fig. 7: Infrared SEDs for different viewing angles (solid line :20°, dashed line: 60°) and dust-to-gas ratios (red: log$\mathcal{D}$=-2.0, blue: log$\mathcal{D}$=-3.6).

views (θ_{view} = 80°), the line-of-sight must traverse the entire torus. This edge-on spectrum (dotted red line) is dominated by the heavily extinguished direct emission from the central engine, producing a fainter SED marked by a deep silicate absorption trough—the classic hallmark of a Type 2 AGN. Thus, by varying a single geometric parameter, our model successfully reproduces the foundational concept of the AGN Unified Model.

2. Accretion Rate ($\dot{m}$)— A Dual Regulator of Engine Power and Torus Structure: In our model, the role of the normalized accretion rate is particularly complex and powerful, extending far beyond that of a simple luminosity scaling factor. It profoundly impacts the torus physics and the resultant spectrum on two distinct levels simultaneously. First, $\dot{m}$ sets the radiative power of the central engine. A higher $\dot{m}$ leads to a more intense central radiation field, which pushes the dust sublimation radius outwards. This is its role as the primary energy input. However, a crucial physical prescription of our model is that $\dot{m}$ is also a direct component of the torus density law, as shown in Eq. (11). As this equation shows, the number density at any point in the torus, $n(r, \theta)$, is directly proportional to $\dot{m}$. This means that increasing $\dot{m}$ not only makes the central engine brighter but also simultaneously makes the entire torus denser and more optically thick. This dual impact results in a complex interplay between the torus's physical structure and its emergent spectrum. For an edge-on, obscured line-of-sight (Type 2), an increase in $\dot{m}$ (moving from left to right in any row) deepens the silicate absorption feature due to the increased density, while at the same time increasing the total re-radiated energy from the torus due to the higher luminosity. Therefore, in our model, $\dot{m}$ is a core parameter that governs both the energy budget and the physical structure of the torus. Its influence on the SED is highly non-trivial, making it an exceptionally important diagnostic of torus physics.

3. DGR and Torus Optical Depth: The DGR reflects the composition of the circumnuclear medium and directly determines its obscuring capability. Examining the grid vertically, the high-DGR case ($log\mathcal{D}$ = −2.0, top row) represents a "classic," dust-rich, and optically thick torus. It is this optically thick structure that makes the viewing angle effects so pronounced. As we move down to the low-DGR case ($log\mathcal{D}$ = −3.6, bottom row), however, the torus becomes tenuous and optically thin. In this scenario, infrared photons can escape easily from any direction, causing the spectra from all viewing angles to nearly coincide and the silicate absorption feature to vanish.

In summary, Fig. 8 is not merely a showcase of our model's capabilities but a deep dive into the physics of AGN in the infrared. It clearly demonstrates that an AGN's IR spectrum is the composite result of its internal physical state and its external viewing geometry.

We performed a spectral decomposition of the mid-infrared (MIR) spectra for a sample of 20 AGNs to constrain the physical properties of their environment. The sample was selected primarily based on Fritz et al. (2006) and Shi et al. (2006), with spectra obtained from the Spitzer Space Telescope's IRS Enhanced Data Products. Our model consists of two primary components: host-galaxy starburst emission and a comprehensive AGN torus template. The AGN component itself includes both thermal reemission from the dust and the attenuated direct radiation from the central engine, with the latter typically being a minor contributor in the mid-infrared. To probe the torus radial structure, we test two dust density laws, $\rho(r) \propto r^{-1}$ and $\rho(r) \propto r^{-2}$.

To find the best-fit model, we decompose each observed MIR spectrum using a linear combination of an AGN template and a starburst template. Specifically, we model the observed flux, $F_{\rm obs}(\lambda)$, as:

$$F_{\rm obs}(\lambda) = A \cdot F_{\rm AGN}(\lambda) + B \cdot F_{\rm SB}(\lambda) \quad (17)$$

where $F_{\rm AGN}(\lambda)$ and $F_{\rm SB}(\lambda)$ are the fluxes of the AGN and starburst templates, and A and B are their respective non-negative scaling coefficients. We iterate through our extensive libraries of templates, and for each AGN-starburst pair, we determine the optimal coefficients using a non-negative least squares (NNLS) fitting routine. The template combination that yields the minimum chi-squared (χ^2) value is then adopted as the best-fit decomposition for that source.

The best-fit models for all sources are presented in Fig. A.1. For each object, the left panel shows the fit using the $\rho(r) \propto r^{-1}$ law, while the right panel corresponds to the fit with the $\rho(r) \propto r^{-2}$ law. The figures clearly display the observed spectrum (black line), the total best-fit model (red line), and the decomposed AGN (blue dashed line) and starburst (green dashed line) components. The detailed best-fit parameters, such as the black hole mass ($M_{\rm BH}$), the accretion rate ($\dot{m}$), and the DGR, are listed in Table A.1 (for the r^{-1} model) and Table A.2 (for the r^{-2} model), respectively.

The two dust density laws, r^{-1} and r^{-2}, produce distinct mid-infrared spectral features in our models, and these differences are key to diagnosing the physical structure of the dusty torus. In general, the steeper density law r^{-2} concentrates dust highly at the inner edge, forming a "hot wall" that tends to produce a narrower, sharper silicate emission peak and struggles to reproduce broad absorption features. In contrast, the shallower density law r^{-1}, with its more extended dust distribution that mixes dust of different temperatures, produces broader, flatter spectral features.

This distinction is clearly reflected in our fitting results. For weak emission sources like Mrk 003, the r^{-2} model produces an overly strong and sharp emission peak that is inconsistent with observations, while the r^{-1} model successfully matches the

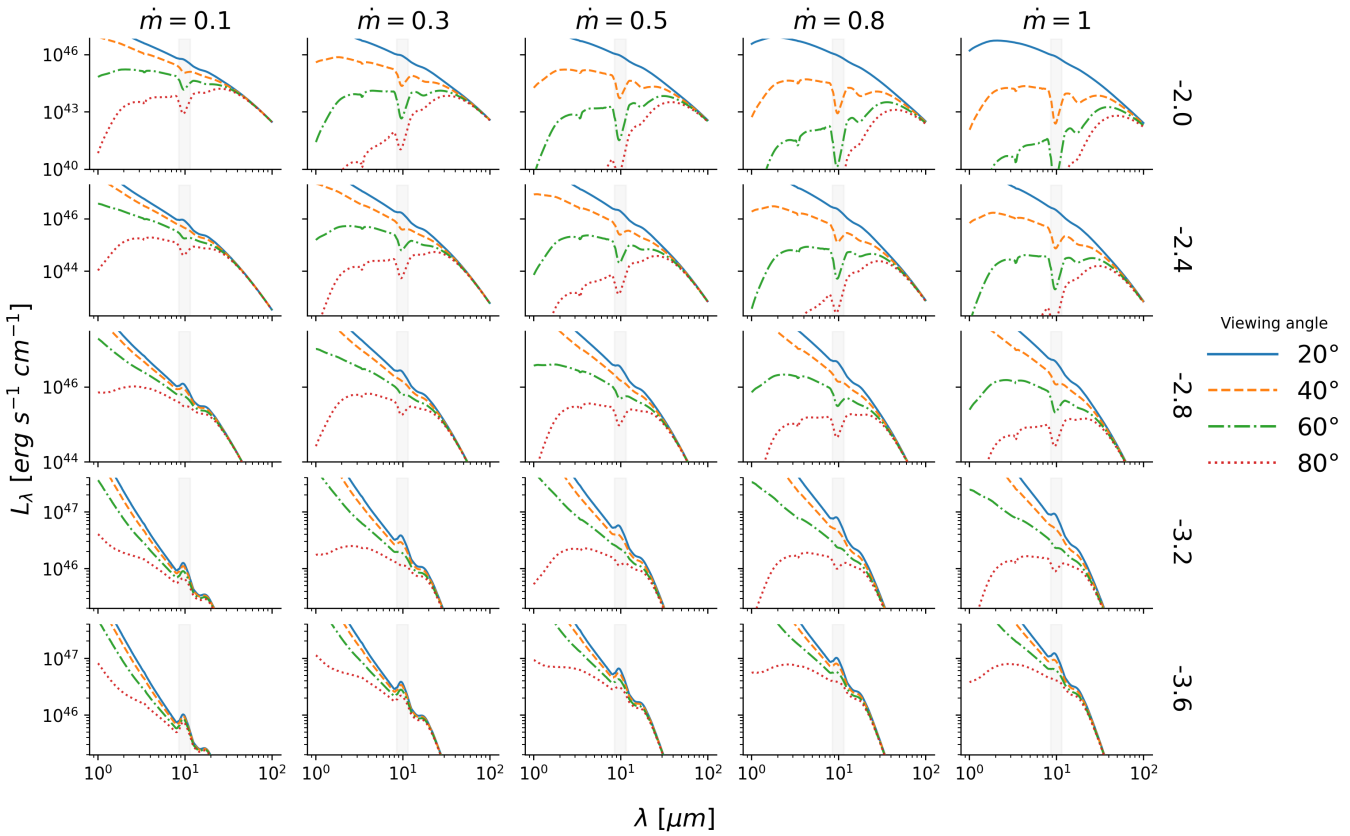

Fig. 8: Grid of rest-frame infrared spectra of the AGN-torus system as a function of accretion rate $\dot{m}$, DGR, and viewing angle θ_{view} for a fiducial black hole mass $M_{\rm BH} = 10^8 M_\odot$. Columns increase in $\dot{m} = 0.1, 0.3, 0.5, 0.8, 1.0$ (left to right); rows increase in $log\mathcal{D} = -3.6, -3.2, -2.8, -2.4, -2.0$ (bottom to top). They are labeled on the right of the figure. In each panel, colored curves show L_λ for $\theta_{view} = 20°, 40°, 60°, 80°$. The vertical dashed line marks the 9.7 μm silicate feature; the shaded band indicates 8–13 μm. All spectra are evaluated on a common rest-frame grid (0.1–100 μm) and plotted with identical vertical scaling per panel.

broader features. For deep absorption sources like Mrk 231, the r^{-2} model lacks sufficient cold dust to produce the obscuration, resulting in an absorption trough that is too shallow and narrow. The r^{-1} model, with its more extended dust distribution, perfectly reproduces the deep and broad absorption features seen in the observations.

This visual assessment is quantitatively confirmed by the goodness-of-fit statistics. A comparison of the reduced chi-squared (χ^2) values, a metric for the goodness of fit, strongly favors the shallower density law. For 18 of the 20 sources in our sample, the $\rho(r) \propto r^{-1}$ model yields a significantly lower χ^2 value. The only exceptions are NGC 7479 and NGC 7172, for which the r^{-2} model provides a better fit.

More importantly, the choice of density law not only affects the goodness-of-fit but also has a substantial impact on the derived physical parameters. A comparison between Table A.1 and Table A.2 reveals that using different density models for the same object can lead to order-of-magnitude differences in key inferred parameters like the black hole mass ($M_{\rm BH}$) and normalized accretion rate ($\dot{m}$). For instance, the derived black hole mass for Mrk 463 is $1 \times 10^7 M_\odot$ with the r^{-1} model, but it becomes $5 \times 10^8 M_\odot$ with the r^{-2} model. This highlights the critical importance of accurately modeling the torus structure for deriving reliable physical parameters of AGN.

Finally, our decomposition also reveals a diversity in the relative contributions of AGN and starburst activity across the sample. In some sources, such as 3C 249.1, the AGN component is absolutely dominant across the entire MIR range. In others, such as Mrk 1014 and Mrk 273, the starburst component makes a very significant contribution, indicating that they are composite systems where an AGN coexists with intense star formation.

In summary, based on both statistical metrics and the quality of the spectral feature fitting, our results strongly support the conclusion that a shallower density law ($\rho(r) \propto r^{-1}$) is a more representative description of the dust distribution in AGN dusty tori studied here.

4. Discussion and conclusions

4.1. A Physically-Motivated 3D Radiative Transfer Model for AGN

A central aspect of this work is the application of a sophisticated 3D radiative transfer model for simulating AGN spectra, which is built upon a physically-motivated parameterization. Specifically, rather than relying on a prescribed, line-of-sight-dependent optical depth, our model utilizes fundamental physical quantities—gas density and the DGR—as its primary inputs. This approach offers significant advantages in physical self-consistency and, crucially, allows for a more direct coupling with the outputs of hydrodynamic and MHD simulations. By treating optical depth as a calculated result instead of an input assumption, our modeling provides a robust bridge between the underlying dynamics of AGN and their observable spectral signatures. While

other contemporary radiative transfer codes also aim for physical realism, our direct parameterization in terms of the wind's density law provides a particularly clear link between the observable SED and the underlying accretion-outflow physics.

A powerful demonstration of this model's capability is its application in constraining the structure of the AGN dusty torus. By leveraging its physical self-consistency, we performed a direct comparison between two competing hypotheses: r^{-1} and r^{-2} density laws. Our fitting results show a clear and statistically significant preference for the r^{-1} distribution. This finding has profound physical implications, as this shallower density law is a key signature of magnetocentrifugal disk winds and reflects a specific scaling of effective viscosity driven by the magnetorotational instability (MRI), which together regulate the unified accretion-outflow process (e.g., Blandford & Payne 1982b; Balbus & Hawley 1991; Lesur 2021). This theoretical framework has been increasingly verified by modern observations across different astrophysical scales (e.g., García-Burillo et al. 2021; Tabone & PDS 70 Team 2022).

4.2. Smooth vs. Clumpy Models

This study employs a smooth medium model, assuming that dust and gas are continuously distributed in space. While much current research suggests that a clumpy model may be more physically realistic in certain aspects—particularly for dust survival in strong radiation fields and for reproducing some detailed spectral features, such as the unexpectedly weak 9.7 μm silicate feature in some unobscured AGNs (e.g., Krolik & Begelman 1988; Feltre et al. 2012; Stalevski et al. 2012)—the adoption of a smooth model in this work is a deliberate choice motivated by several key advantages.

We adopt a smooth density distribution for two primary reasons. First, its computational efficiency allows us to extensively explore the impact of fundamental parameters, such as the large-scale density law (r^{-1} vs. r^{-2}). Second, a smooth model has fewer free parameters compared to clumpy models, which must also specify properties like the volume filling factor, the number of clumps, and the density structure within each clump. This simplicity provides a clearer link between the model's core assumptions and its spectral predictions, making our results easier to interpret and less ambiguous.

Therefore, our smooth model serves as a crucial foundational baseline to first isolate and test the primary effect of the large-scale density law. Having established the clear preference for the density law r^{-1} within this well-defined framework, future work can build directly upon this result by incorporating clumps to investigate its secondary effects on the spectral energy distribution.

4.3. Limitations

Despite the success of our physically-motivated model in discriminating between density laws, we acknowledge several simplifications that define avenues for future work. First, our model explores the effects of a simplified set of key physical parameters, including the black hole mass ($M_{\rm BH}$), normalized accretion rate ($\dot{m}$), DGR, viewing angle, dust sublimation temperature, etc. However, this is a simplified physical picture. For instance, our model assumes an axisymmetric and flared disk structure, which neglects potential asymmetries or warps that could influence the spectra. The treatment of the host galaxy starburst is also simplified, as we account for its contribution by adding a generic template during the fitting process. This template may not be universally applicable, which could introduce a bias in our final fitted parameters, particularly for AGN where the host galaxy's contribution is substantial, potentially causing our fit to overestimate the AGN torus temperature or dust mass to compensate for a template mismatch.

Second, a key assumption is a constant DGR throughout the model volume. In reality, the DGR in an AGN dusty torus could vary significantly due to metallicity gradients, dust formation and destruction (Sarangi et al. 2019). Including a DGR that changes with location is a critical next step to enhance the model's physical realism.

Third, an analysis of the best-fit parameter distributions in Tables A.1 and A.2 reveals potential systematic trends that warrant discussion. A majority of our sources are best-fit with high viewing angles ($\theta_{view} \geq 60°$). While this may partly reflect an observational selection bias in the parent sample toward obscured, Type 2 objects (Fritz et al. 2006; Shi et al. 2006), it could also indicate a degeneracy within our model where edge-on geometries are favored to produce even moderate levels of extinction.

Furthermore, a visual inspection of the fits in Fig. A.1 suggests that our model is particularly successful at reproducing strong, deep 9.7 μm silicate absorption features. Conversely, it appears to have more difficulty precisely matching the weak silicate emission features seen in some less obscured sources. This may be a limitation tied to several of our physical assumptions. It could be a consequence of the smooth density distribution, which might struggle to model the complex radiative transfer in the optically thin, hot inner regions where the emission originates. Alternatively, or in addition, it could point to a limitation in our adopted dust component; the specific grain sizes and optical properties of the ISM-like dust used in our model may not fully capture the emissivity of the hot dust grains that dominate the emission near the sublimation front. Future work incorporating a clumpy medium and exploring more diverse dust compositions could address these aspects.

Finally, our analysis was based on normalized spectra from low-redshift ($z < 1$) AGN. This method is powerful for isolating spectral features, but it discards absolute flux information, which means we cannot independently constrain physical parameters like the total luminosity or mass. A key future goal for our model is to extend this analysis to high-redshift ($z > 1$) AGN, where a full multi-wavelength SED fitting will be required to get a complete picture of the system. Therefore, a crucial next step is to apply this framework to the full, unnormalized SEDs of both local and high-redshift AGN to fully exploit its predictive power.

4.4. Summary and Implications

In summary, this study applies a sophisticated 3D radiative transfer model for AGN, which is built on fundamental physical parameters, and demonstrates its power by showing that a r^{-1} density law provides a superior fit to observational data. This result profoundly links the AGN structure to MHD-driven accretion-outflow mechanisms. Crucially, this provides strong evidence for a scenario where the AGN torus is an active site of dust formation, offering a compelling physical mechanism to help resolve the long-standing dust budget crisis (e.g., Ferrara et al. 2017). If this wind structure is typical, the same process could explain the massive dust reservoirs seen in the earliest quasars (e.g., Wang et al. 2023; Valiante et al. 2011), fundamentally shaping our understanding of early galaxy growth.

The work's dual contribution—providing both an advanced modeling tool and a specific physical constraint on AGN the-

ory—paves the way for the next generation of more realistic simulations. A key implication is that physical parameters like black hole mass and accretion rate, when derived using simpler torus models, may be subject to significant systematic biases. Our validated r^{-1} model thus provides a more reliable tool for interpreting the wealth of high-quality mid-infrared spectra from JWST. Future work should focus on incorporating even more complex physics, such as a clumpy medium, into this modeling framework. Furthermore, the distinct kinematics predicted by MHD wind models ($v(r) \propto r^{-0.5}$) (e.g., Blandford & Payne 1982a; Fukumura et al. 2010; Sarangi et al. 2019) offer a clear avenue for observational verification with high-resolution gas velocity maps from facilities like ALMA, which would provide a definitive test of the physical scenario favored by our work.

References

Aalto, S. et al. 2020, A&A, 640, A104
Antonucci, R. 1993, ARA&A, 31, 473
Antonucci, R. R. J. & Miller, J. S. 1985, ApJ, 297, 621
Balbus, S. A. & Hawley, J. F. 1991, ApJ, 376, 214
Behar, E. et al. 2009, ApJ, 703, 1347
Blandford, R. D. & Payne, D. G. 1982a, MNRAS, 199, 883
Blandford, R. D. & Payne, D. G. 1982b, MNRAS, 199, 883
Bogdanović, T. et al. 2021, ApJ, 907, 88
Brandl, B. R., Bernard-Salas, J., Spoon, H. W. W., et al. 2006, ApJ, 653, 1129
Chan, C.-H. et al. 2017, MNRAS, 469, 950
Dale, D. A., Aniano, G., Engelbracht, C. W., et al. 2012, ApJ, 745, 95
Done, C., Davis, S. W., Jin, C., Blaes, O., & Ward, M. 2012, MNRAS, 420, 1848
Donnan, C. T. et al. 2023, NatAs, 7
Downes, D. & Solomon, P. M. 1998, ApJ, 507, 615
Draine, B. T. 2003, ARA&A, 41, 241
Draine, B. T. 2011, Physics of the Interstellar and Intergalactic Medium (Princeton: Princeton University Press)
Draine, B. T. & Hensley, B. S. 2021, ApJ, 909, 94
Draine, B. T. & Li, A. 2007, ApJ, 657, 810
Dwek, E. 1987, ApJ, 322, 812
Dwek, E. & Cherchneff, I. 2011, ApJ, 727, 63
Elvis, M. 2000, ApJ, 545, 63
Elvis, M. et al. 1994, ApJS, 95, 1
Elvis, M. et al. 2002, ApJ, 567, L107
Feltre, A., Hatziminaoglou, E., Fritz, J., & Franceschini, A. 2012, MNRAS, 426, 120
Ferrara, A. et al. 2017, MNRAS, 468, 1257
Forbes, D. A. & Ponman, T. J. 1999, MNRAS, 309, 623
Förster Schreiber, N. M., Genzel, R., Lutz, D., Sternberg, A., et al. 2003, A&A, 399, 833
Fritz, J., Franceschini, A., & Hatziminaoglou, E. 2006, MNRAS, 366, 767
Fukumura, K., Kazanas, D., Contopoulos, I., & Behar, E. 2010, ApJ, 715, 636
Fukumura, K. et al. 2018, ApJ, 853, 46
Gallimore, J. F. et al. 2016, ApJ, 829, 7
García-Burillo, S. et al. 2021, A&A, 652, A98
Genzel, R., Lutz, D., Sturm, E., et al. 1998, ApJ, 498, 579
Haardt, F. & Maraschi, L. 1993, ApJ, 413, 507
Hauser, M. G. & Dwek, E. 2001, ARA&A, 39, 249
Hensley, B. S. & Draine, B. T. 2023, ApJ, 948, 55
Holczer, T., Behar, E., & Kaspi, S. 2007, ApJ, 663, 799
Jaffe, W. et al. 2004, Nature, 429, 47
Jones, A. P. & Nuth, J. A. 2011, A&A, 530, A44
Kormendy, J. & Ho, L. C. 2013, ARA&A, 51, 511
Krolik, J. H. & Begelman, M. C. 1988, ApJ, 329, 702
Laurent, O., Mirabel, I. F., Charmandaris, V., et al. 2000, A&A, 359, 887
Lawrence, A. & Elvis, M. 2010, ApJ, 714, 561
Lesur, G. 2021, A&A, 650, A65
Li, J. et al. 2023, ApJ, 944, 76
Lopez-Rodriguez, E. et al. 2020, ApJ, 893, 33
Lusso, E., Worseck, G., Hennawi, J. F., et al. 2016, MNRAS, 456, 1253
López-Gonzaga, N. & Jaffe, W. J. 2016, MNRAS, 462, 4183
Mathis, J. S., Rumpl, W., & Nordsieck, K. H. 1977, ApJ, 217, 425
Nardini, E., Risaliti, G., Salvati, M., et al. 2008, MNRAS, 385, L130
Nenkova, M., Sirocky, M. M., Ivezić, Ž., & Elitzur, M. 2008, ApJ, 685, 147
Netzer, H. 1987, MNRAS, 225, 55
Netzer, H. 2013, The Physics and Evolution of Active Galactic Nuclei (Cambridge: Cambridge University Press)
Osterbrock, D. E. & Ferland, G. J. 2006, Astrophysics of Gaseous Nebulae and Active Galactic Nuclei, 2nd edn. (Sausalito: University Science Books)
Pier, E. A. & Krolik, J. H. 1992, ApJ, 401, 99
Polletta, M., Tajer, M., Maraschi, L., et al. 2007, ApJ, 663, 81
Radovich, M., Kahanpää, J., & Lemke, D. 2001, A&A, 377, 73
Rees, M. J. 1984, ARA&A, 22, 471
Reynolds, C. S. 2013, Space Sci. Rev., 183, 277
Rémy-Ruyer, A., Madden, S. C., Galliano, F., , et al. 2014, A&A, 563, A13
Sanders, D. B. & Mirabel, I. F. 1996, ARA&A, 34, 749
Sarangi, A., Dwek, E., & Kazanas, D. 2019, ApJ, 885, 126
Shakura, N. I. & Sunyaev, R. A. 1973, A&A, 24, 337
Shi, Y. et al. 2006, ApJ, 653, 127
Silva, L., Granato, G. L., Bressan, A., & Danese, L. 1998, ApJ, 509, 103
Spoon, H. W. W., Marshall, J. A., Houck, J. R., et al. 2007, ApJ, 654, L49
Srinivasan, S. et al. 2017, ApJ, 836, 7
Stalevski, M., Fritz, J., Baes, M., Nakos, T., & Popović, L. Č. 2012, MNRAS, 420, 2756–2772
Tabone, B. & PDS 70 Team. 2022, A&A, 665, A4
Tielens, A. G. G. M. 2005, The Physics and Chemistry of the Interstellar Medium (Cambridge: Cambridge University Press)
Tristram, K. R. W. et al. 2007, A&A, 474, 837
Valiante, R. et al. 2011, MNRAS, 416, 1916
Veilleux, S. et al. 2020, A&A Rev., 28, 2
Wada, K. 2012, ApJ, 758, 66
Wada, K. et al. 2009, ApJ, 702, 63
Wang, R. et al. 2023, ApJ, 945, L12
Zubko, V., Dwek, E., & Arendt, R. G. 2004, ApJS, 152, 211

Appendix A: Supplementary tables and figures

Table A.1: Best-fit results (AGN density law $\rho(r) \propto r^{-1}$)

Object	χ^2	$M_{\rm BH}$	$\dot{m}$	DGR	θ_{view}	SB	A	B
3C 249.1	2.35	5×10^8	0.8	$10^{-3.6}$	60	Mrk 52	0.834	0.016
3C 445	2.30	5×10^8	0.8	$10^{-3.6}$	60	Mrk 52	0.919	0.034
Mrk 1014	20.16	5×10^8	0.1	$10^{-3.4}$	80	NGC 253	0.609	1.016
Mrk 003	11.08	5×10^7	1.0	$10^{-2.8}$	80	Mrk 52	0.477	0.230
Mrk 1066	1.44	1×10^7	0.3	$10^{-2.2}$	80	NGC 4194	0.195	0.877
Mrk 231	5.56	5×10^8	0.5	$10^{-3.2}$	80	Arp 220	0.919	0.604
Mrk 273	1.60	5×10^8	0.5	$10^{-2.2}$	60	NGC 2623	0.252	0.706
Mrk 463	1.02	1×10^7	0.1	$10^{-2.2}$	80	NGC 3310	0.896	0.125
Mrk 506	11.24	1×10^8	0.5	$10^{-3.2}$	80	NGC 3310	0.659	0.176
NGC 2110	3.65	5×10^7	0.5	$10^{-2.6}$	80	NGC 520	0.829	0.193
NGC 4507	2.14	1×10^8	0.5	$10^{-3.2}$	80	NGC 3310	0.989	0.269
NGC 4941	11.57	1×10^8	0.8	$10^{-3.0}$	80	NGC 3310	0.562	0.317
NGC 5643	5.96	5×10^7	1.0	$10^{-2.8}$	80	NGC 3310	0.441	0.848
NGC 6240	4.80	1×10^8	0.3	$10^{-2.0}$	60	NGC 3556	0.246	0.761
NGC 7172	2.33	1×10^8	1.0	$10^{-2.4}$	40	NGC 4194	0.928	0.148
NGC 7213	11.67	5×10^8	0.3	$10^{-3.6}$	80	Mrk 52	0.871	0.239
NGC 7479	1.52	5×10^8	0.8	$10^{-2.6}$	60	NGC 520	0.872	0.269
PG 2130+099	0.95	1×10^8	0.8	$10^{-3.2}$	60	Mrk 52	0.959	0.055
PICA	9.42	5×10^8	1.0	$10^{-3.8}$	80	Mrk 52	0.907	0.168
UGC 04013	8.15	1×10^8	0.8	$10^{-3.2}$	80	NGC 3310	0.823	0.384

Table A.2: Best-fit results (AGN density law $\rho(r) \propto r^{-2}$)

Object	χ^2	$M_{\rm BH}$	$\dot{m}$	DGR	θ_{view}	SB	A	B
3C 249.1	4.57	5×10^8	1.0	$10^{-3.6}$	80	Mrk 52	0.848	0.165
3C 445	6.80	1×10^8	0.3	$10^{-3.0}$	80	Mrk 52	0.954	0.168
Mrk 003	33.86	5×10^7	0.5	$10^{-2.0}$	80	Mrk 52	0.367	0.531
Mrk 1014	41.73	5×10^8	0.1	$10^{-3.2}$	80	NGC 253	0.710	1.097
Mrk 1066	1.72	5×10^7	0.8	$10^{-2.0}$	60	NGC 4818	0.180	0.869
Mrk 231	13.53	1×10^8	0.3	$10^{-3.0}$	80	NGC 253	0.899	0.674
Mrk 273	1.85	5×10^8	1.0	$10^{-2.4}$	80	NGC 2623	0.249	0.716
Mrk 463	4.12	1×10^8	1.0	$10^{-3.0}$	80	Mrk 52	0.852	0.299
Mrk 506	17.83	5×10^8	0.3	$10^{-3.0}$	60	Mrk 52	0.734	0.420
NGC 2110	7.65	5×10^7	0.3	$10^{-3.0}$	80	Mrk 52	0.830	0.389
NGC 4507	12.59	5×10^8	0.1	$10^{-3.4}$	80	Mrk 52	1.011	0.541
NGC 4941	22.22	1×10^8	0.5	$10^{-3.0}$	80	Mrk 52	0.516	0.788
NGC 5643	12.32	1×10^7	1.0	$10^{-2.0}$	80	Mrk 52	0.323	0.912
NGC 6240	4.84	5×10^8	0.1	$10^{-2.0}$	80	NGC 3556	0.241	0.772
NGC 7172	1.69	5×10^8	1.0	$10^{-2.0}$	40	NGC 4194	0.961	0.241
NGC 7213	32.11	5×10^8	0.3	$10^{-3.4}$	80	Mrk 52	0.951	0.407
NGC 7479	0.71	5×10^8	0.3	$10^{-2.2}$	80	NGC 520	0.863	0.380
PG 2130+099	2.89	5×10^7	0.3	$10^{-2.8}$	80	Mrk 52	0.945	0.228
PICA	34.06	5×10^8	0.8	$10^{-3.6}$	80	Mrk 52	0.968	0.389
UGC 04013	15.44	5×10^8	0.5	$10^{-3.2}$	80	Mrk 52	0.757	0.690

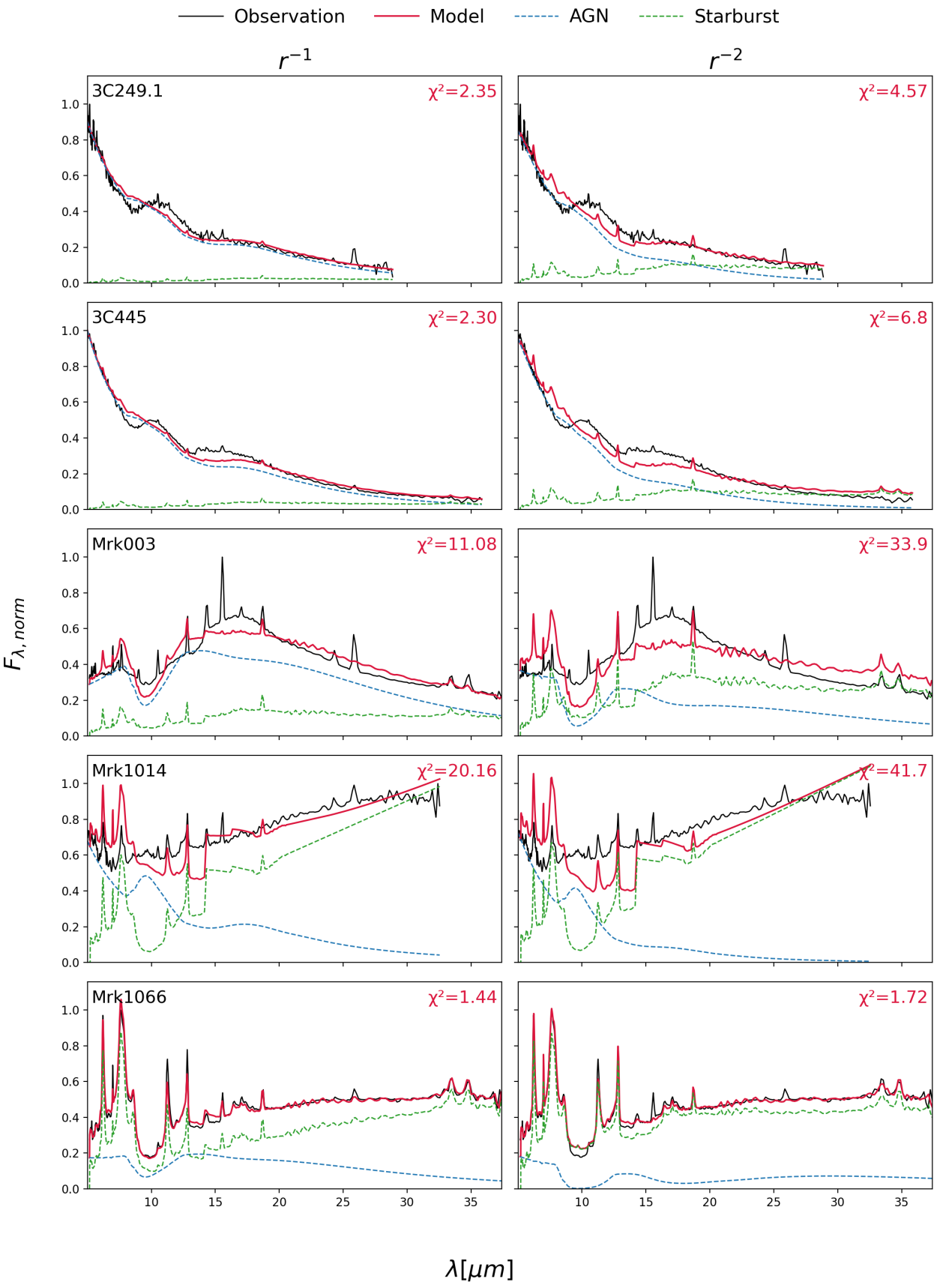

Fig. A.1: Fitting results of MIR observational spectra with our models. For each target, the left panel uses AGN templates with density law $\rho(r) \propto r^{-1}$, while the right panel uses $\rho(r) \propto r^{-2}$. Black curves show the observed, normalized F_λ spectra; the red solid curve is the combined model; blue and green dashed curves denote the AGN and starburst components, respectively. The χ^2 of each fit is indicated in the upper-right of each subpanel.

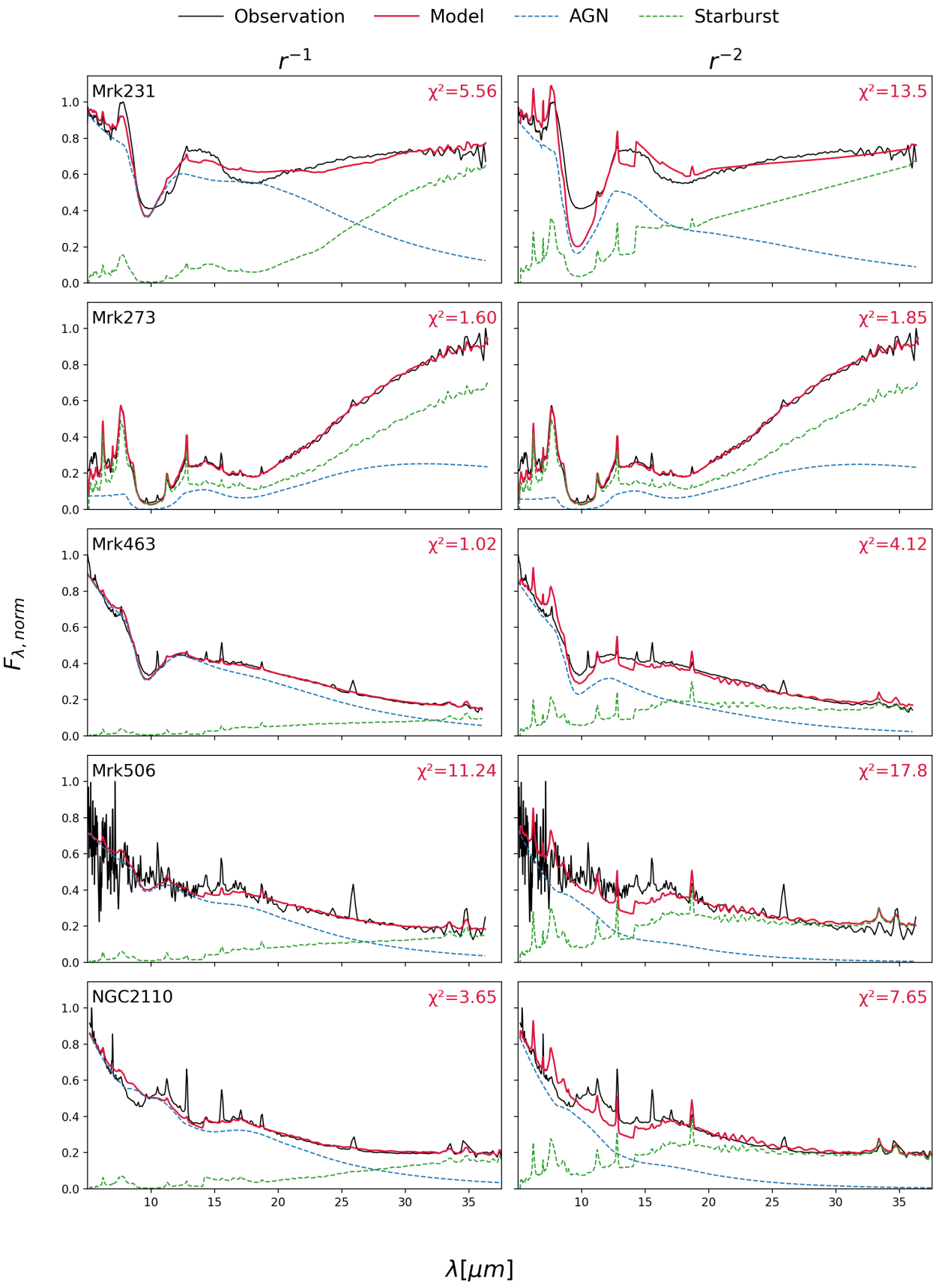

Fig. A.1: Continued

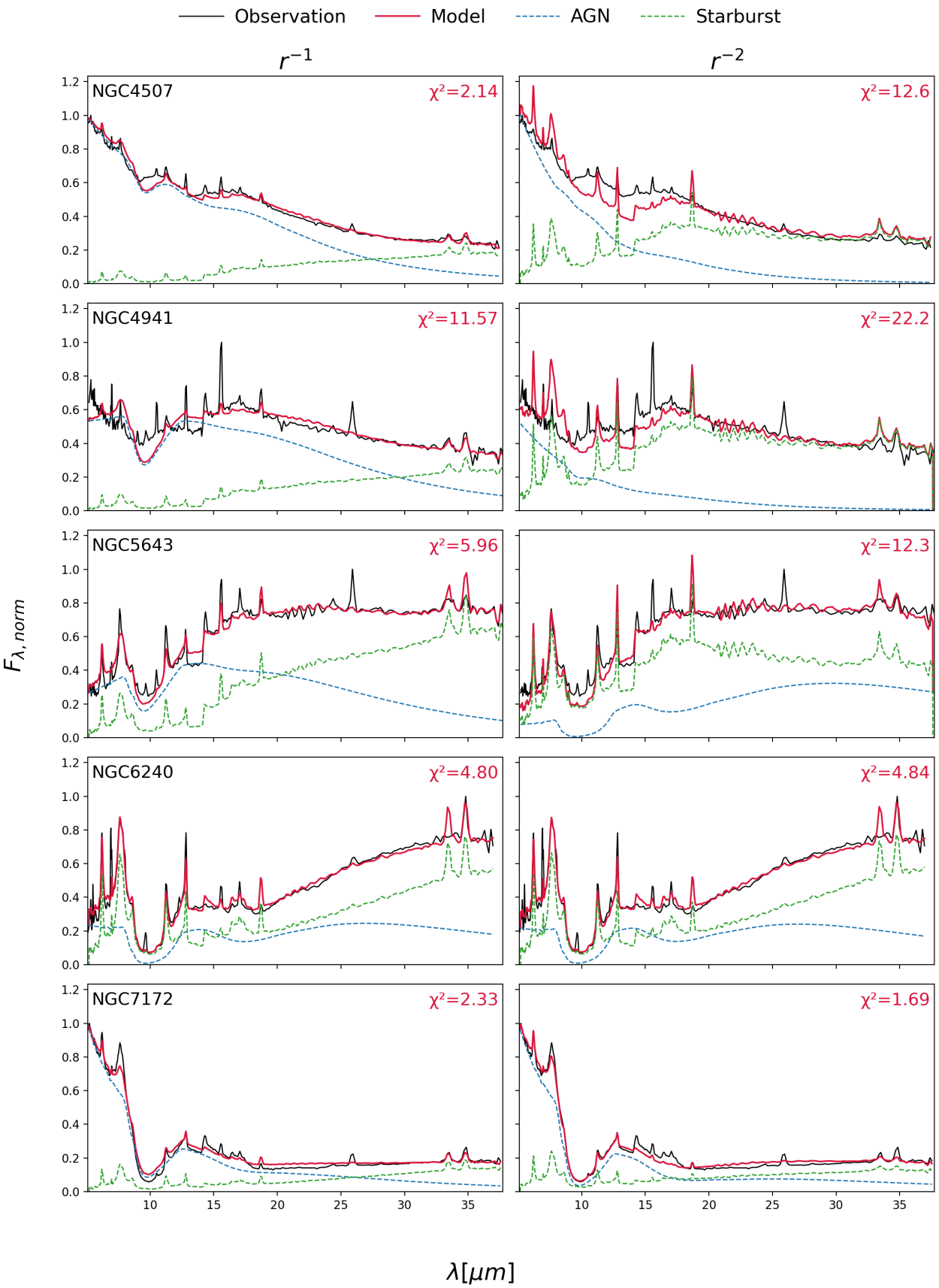

Fig. A.1: Continued

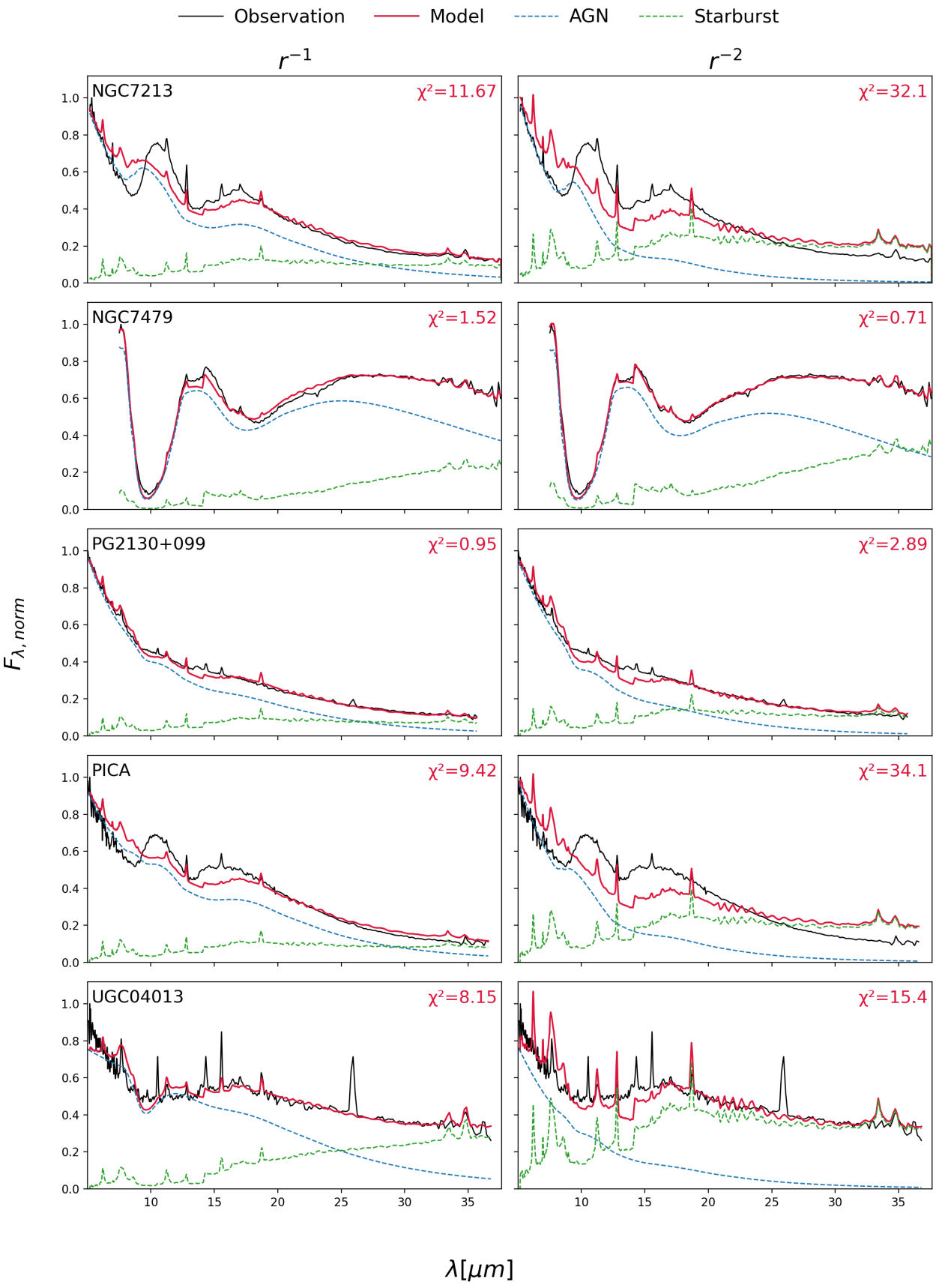

Fig. A.1: Continued